# **Inorganic Chemistry**

pubs.acs.org/IC Article

## On the Electrochemical Phase Evolution of Anti-PbO-Type CoSe in Alkali Ion Batteries

Conrad H. R. Gillard, Xiuquan Zhou, Maxim Avdeev, Efrain E. Rodriguez, and Neeraj Sharma\*



Cite This: Inorg. Chem. 2021, 60, 7150-7160



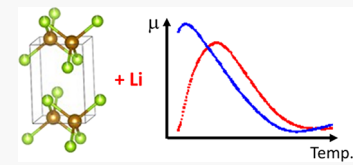
**ACCESS** 

Metrics & More

Article Recommendations

Supporting Information

**ABSTRACT:** The reaction mechanism of anti-PbO type CoSe in Li, Na, and K ion half cells is studied. Ex situ X-ray diffraction data is analyzed with the Rietveld method, in conjunction with discharge profiles and extended cycling data. These indicate that intercalation followed by a conversion reaction occur in all systems. For the case of Na, the intercalation reaction was associated with a contraction in the stacking axis lattice parameter, whereas Li and K exhibited expansion. Magnetic susceptibility versus temperature measurements of Li- and Na-intercalated CoSe samples produce unusual results, and several explanations are proposed, including the



formation of a superconductive phase. Extended cycling experiments are also performed, and high initial capacities of 937, 657, and 972 mAh/g are observed for Li, Na, and K, respectively. However, all systems exhibit significantly lower second discharge capacities of 796, 530, and 515 mAh/g. The capacities continue to decline during extended cycling, with the systems exhibiting tenth cycle capacity fades of 52, 85, and 95% and Li half cells exhibit capacities over 150 mAh/g at 15 mA/g after 50 cycles. The capacity fade is likely attributable to volume changes and irreversibility associated with conversion and intercalation reactions. This work correlates electrochemical features to the structural evolution, magnetic properties, and reaction mechanisms.

Anti-PbO type CoSe has recently been synthesized via the topochemical de-intercalation of  $K_xCo_2Se_2$ . The anti-PbO-type crystal structure (space group P4/nmm) is comprised of layers of edge-sharing  $CoSe_4$  tetrahedra. These quasi-2D layers are stacked along the c crystallographic axis and are separated by van der Waals gaps. Due to the predominance of covalent bonding within layers, the intralayer bonding is relatively strong compared to the interlayer forces.

As a consequence of this layered crystal structure, anti-PbOtype materials have exhibited the capacity to host intercalating species.<sup>2–14</sup> Intercalation induces a deviation of the electron doping level from its initial neutral state and has been shown to profoundly affect the electronic properties. Particularly, significant modifications were observed in the case of anti-PbO-type FeSe, which has a superconducting critical temperature  $(T_c)$  of 8 K. Doping this material with 0.15-0.20 electrons per Fe atom, using intercalated alkali cations, Li/ amides, or LiOH, resulted in drastically enhanced  $T_c$  values of 35-44 K. 8,9,11,12,15 Similarly, for the case of FeS, an increase in  $T_{\rm c}$  from 4 to 8 K was reported following LiOH intercalation. The above processes are redox reactions involving intercalation and are therefore reminiscent of the reactions that occur in rechargeable battery electrodes. As a result, electrochemical modification provides a direct and possibly cleaner approach to tune the Fermi level.

Apart from FeSe and FeS, no layered metal chalcogenides exhibiting the same anti-PbO-type structure were reported until the recent discovery of CoSe and CoS.<sup>1</sup> CoSe is weakly ferromagnetic with a Curie temperature of 10 K. However, in solid-state synthesized KCo<sub>2</sub>Se<sub>2</sub>, this transition temperature is markedly higher, occurring at 82 K.<sup>1</sup> These property changes

were attributed to the depopulation of an electronic antibonding band, driven by a decrease in the oxidation state of Co from +2 in CoSe to +1.5 in  $KCo_2Se_2$ .<sup>1</sup> Consequently, an investigation into the direct electrochemical modification of CoSe is intriguing, with regard to the effects on the structure and properties. Furthermore, such an investigation constitutes another platform for comparison with the Fe-based superconductors.

Research interest in anti-PbO type materials has not been confined to their magnetic properties; their performance as Li and Na ion battery electrodes has also been studied.<sup>2–4,18</sup> All investigations reached similar conclusions regarding phase evolution. Specifically, an intercalation reaction was found to occur at shallow discharge states, followed by a conversion reaction at deeper discharge states. The general forms of these reactions are given in eqs 1 and 2:

$$2MCh + xA^{+} + xe^{-} \rightarrow A_{x}M_{2}Ch_{2}$$
 (1)

$$A_x M_2 Ch_2 + (4 - x)A^+ + (4 - x)e^- \rightarrow 2A_2 Ch + 2M$$
(2)

in which M denotes a metal, Ch denotes a chalcogen, and A denotes an alkali metal. These studies reported minimal

Received: January 23, 2021 Published: April 26, 2021





capacity fade; however, it should be noted that nanostructuring and/or narrow voltage windows were employed in all cases.<sup>2–4</sup>

It should also be noted that in this work, the term "discharge" is used to refer to the spontaneous reaction that occurs within a battery when the external circuit is closed, as is conventional in the electrochemical literature. <sup>19</sup> As can be seen in eqs 1 and 2, it is correlated to a reduction of the *M* species. In this work, we refer to discharge within an electrochemical cell rather than reduction.

Anti-PbO-type materials have also exhibited unusual behavior when utilized as alkali ion battery electrodes. For example, both FeS and FeSe have shown an increase in capacity over the first few cycles in Li ion batteries for reasons that are not fully understood.<sup>2,3</sup> Furthermore, discharge capacities in excess of twice the theoretical limit of 398 mAh/g, based on the above conversion reaction, were reported for the case of FeSe versus Li.<sup>2</sup>

In the present work, the behavior of anti-PbO-type CoSe in alkali ion batteries was investigated. Lithium, sodium, and potassium ion batteries were constructed, and extended cycling experiments were performed. Ex situ powder X-ray diffraction (PXRD) and magnetic susceptibility data were collected at various states of discharge. Based on the Rietveld analysis of this PXRD data and electrochemical performance, the phase evolution of CoSe during the first discharge process was elucidated. This was briefly correlated to the evolution of the magnetic properties. Regions of the discharge profile were correlated to specific reactions, such as the intercalation process.

## **■ EXPERIMENTAL SECTION**

Construction and Disassembly of Batteries. Anti-PbO-type CoSe was synthesized using a newly developed topochemical deintercalation reaction, which is described in detail in the literature. Slurries were prepared by combining an 8:1:1 ratio of ground active material, CoSe:carbon black:polyvinylidene fluoride. N-Methyl-2pyrrolidone was added until a thick slurry was produced, and the mixture was magnetically stirred in an argon glovebox for 24 h. Subsequently, the slurry was cast onto copper foil using a doctor blade, dried under argon, and pressed at 100 kPa for 1 h. The resultant electrode sheets were used to construct lithium, sodium, and potassium metal half-cells, following standard literature methods.<sup>15</sup> The stainless steel CR2032 coin cell cases, wave springs, and spacers were all purchased from MTI. A 1 M LiPF<sub>6</sub>, 1 M NaPF<sub>6</sub>, and 0.8 M KPF<sub>6</sub> dissolved in an equivolumetric mixture of ethylene carbonate (EC) and dimethyl carbonate (DMC) were used as electrolytes for lithium, sodium, and potassium metal half cells, respectively. Following construction, each battery was rested for 24 h then galvanostatically discharged, or in some cases cycled, at a current density of 15 mA/g using a Neware battery cycler. The batteries were discharged to a targeted state after which they were immediately transferred to an argon-filled glovebox and disassembled. The electrodes were removed and washed with DMC in order to remove any electrolyte solution, and salts adhered to the surface and left for 24-48 h to allow any residual DMC to evaporate.

It should be noted that PVDF binder and EC/DMC solvent were selected in order to be consistent with studies on similar materials, such as anti-PbO-type FeSe.<sup>2,4</sup> However, the use of polytetrafluoroethylene (PTFE) binder may enable the use of current-collector free electrodes or produce different electrochemical behaviors. Consequently, such experiments are proposed for future works. Additionally, it should be noted that propylene carbonate (PC) and ethyl carbonate/diethyl carbonate (EC/DEC) were investigated as electrolyte solvents for the electrochemical intercalation of sodium within anti-PbO type FeSe.<sup>7</sup> EC/DEC did not co-intercalate with sodium; however, PC did, and it induced significant changes to the magnetic

properties of FeSe. Consequently, experiments with these two solvents are proposed for future works.  $^{7}$ 

Analytical Methods. Powder X-ray diffraction (PXRD) was used to investigate the phase evolution of the electrodes. Diffraction patterns were collected using either a Stoe Stadi P, Panalytical Empyrean, or Panalytical MRD Scherrer diffractometer, utilizing Mo, Co, Ag or Cu K $\alpha$  radiation. In the case of Cu and Co radiation, the electrode material was scraped off the current collector and transferred to an air-sensitive sample holder. The sample was not ground, and the sample holder was sealed before being removed from the Ar glovebox. In the case of Mo and Ag radiation, the sample was ground and transferred to a capillary, which was sealed with wax before removal from the Ar glovebox. The Rietveld method was used to refine structural models with the PXRD data, using the General Structural Analysis System-II (GSAS-II) software package.<sup>20</sup> A Quantum Design EverCool-II 9 T PPMS with the vibrating sample magnetometry option was used to measure magnetic susceptibility data from powder samples. Temperature-dependent magnetic susceptibility data was collected under zero-field-cooled (ZFC) and field-cooled (FC) conditions upon warming from 3 to 300 K, with an applied field of 300 Oe.

## RESULTS AND DISCUSSION

Structural Characterization of the Electrode. PXRD data of an electrode was analyzed with the Rietveld method, as presented in Figure 1. Refinement of the anti-PbO type CoSe (henceforth tetragonal CoSe) structural model resulted in close alignment between the calculated reflection markers and peaks in the measured data. The lattice parameters for

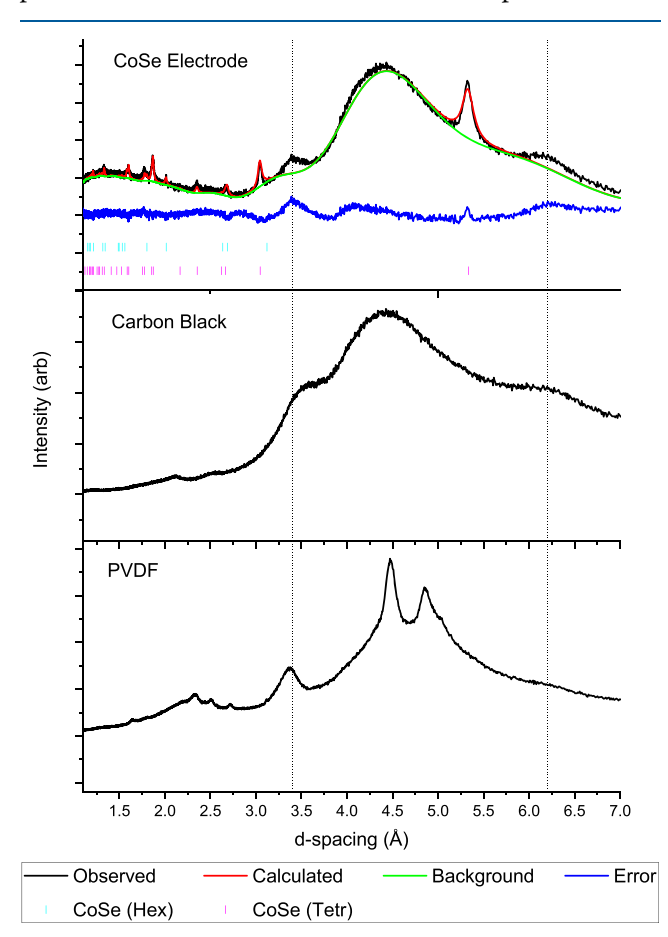


**Figure 1.** PXRD data of the CoSe electrode, carbon black, and PVDF. The Rietveld-refined fit of the hexagonal and tetragonal structural models of CoSe to the PXRD data of the CoSe electrode are shown.

Table 1. Rietveld Refined Model Parameters of CoSe from the Literature<sup>1</sup> and as a Processed Electrode

sample	CoSe a (Å)	CoSe c (Å)	wR
literature	3.717(3)	5.330(3)	2.10%
electrode	3.172(2)	5.330(3)	2.96%

tetragonal CoSe showed no statistically significant difference compared to those published in the literature, as shown in Table 1, indicating minimal structural change during electrode casting. An intensity mismatch was observed, so the March-Dollase ratio was refined, which significantly improved the intensity agreement, indicating the presence of preferred orientation, likely attributable to doctor blading during the casting process. The refinement of atomic displacement parameters was found to give only a marginal improvement in the statistical fit, so these were left fixed at their initial values. In order to maintain consistency, the same parameters were refined in all Rietveld analyses in this work. That is, the March-Dollase ratio with the same unique axis (001) was refined, and the atomic displacement parameters were kept constant. An unmatched peak at a d-spacing of 2.01 Å was also observed. Hexagonal CoSe was used as a precursor during the synthesis of tetragonal CoSe, so the structural model for this phase was included, resulting in a match for this peak. Broad peaks were also observed at d = 6.25 and 3.4 Å, indicating the

presence of an amorphous or nanocrystalline component. PXRD patterns from carbon black and PVDF were collected, which exhibited similar broad peaks at d=6.2 and 3.4 Å respectively. In all cases, a sloping background was present, likely attributable to the Kapton foil used in the sample holder. More detailed figures of the Rietveld analysis of the electrode are given in Figures S1 and S2.

Electrochemical Performance. Charge—discharge curves and extended cycling capacity plots are presented in Figure 2. Large initial capacities of 937, 657, and 972 mAh/g were observed in the Li, Na, and K systems respectively. These values all significantly exceeded the theoretical capacity of 389 mAh/g, based on the consumption of two alkali metal ions per CoSe functional unit, via the conversion reaction given in eq 2. Note that the oxidation state of Co in CoSe is 2+, so the conversion reaction to metallic Co would require the transfer of 2 Li<sup>+</sup>. These results are consistent with past studies on anti-PbO-type FeS<sup>3</sup> and FeSe<sup>2,4</sup> batteries, which have also reported above-theoretical capacities in early cycles. Each of these studies ascribed this excess capacity to the formation of a solid electrolyte interface and decomposition of the electrolyte.

All systems exhibited poor cycle life, with second discharge capacities of 796, 530, and 515 mAh/g and tenth cycle capacity decreases of 52, 85, and 95%, respectively. This differs from published results on anti-PbO type batteries, which reported

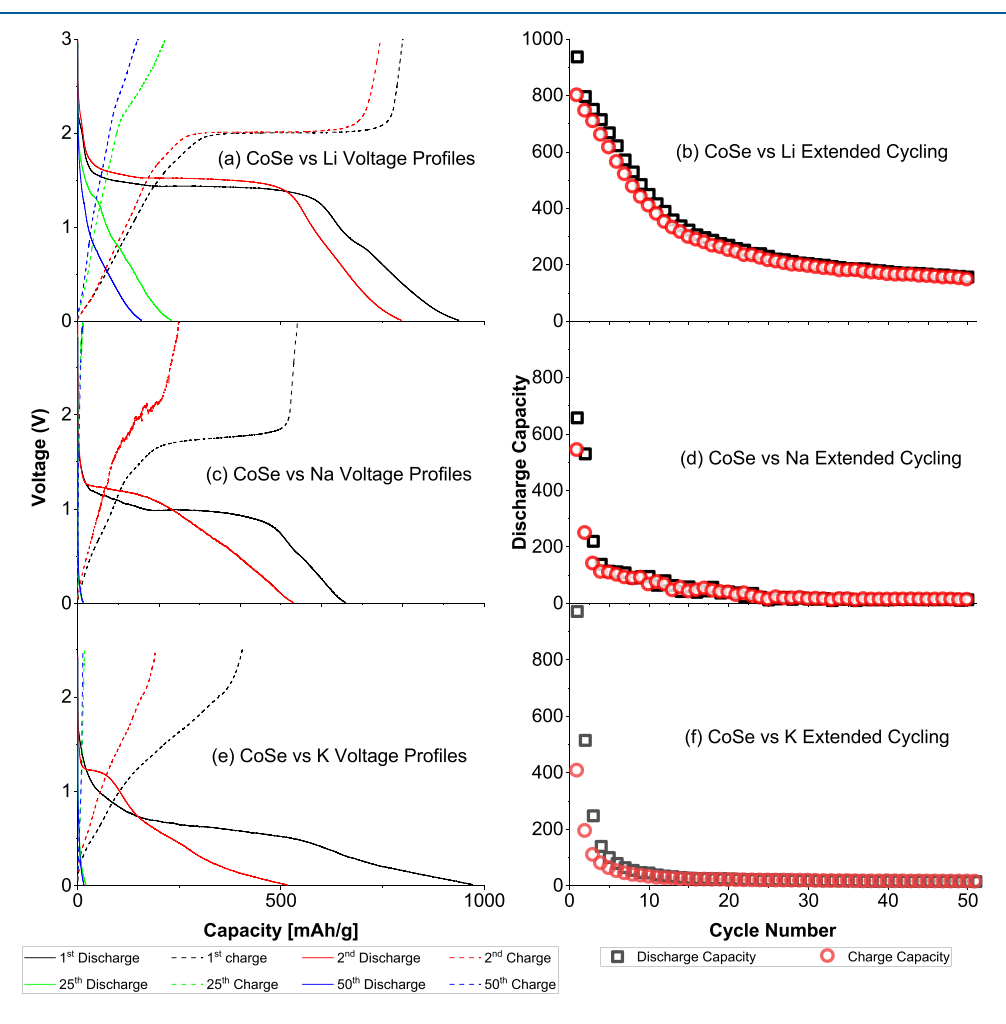


Figure 2. Selected discharge—charge curves (a, c, e) and capacity versus cycle number plots (b, d, f) for CoSe versus Li Na and K half cells, respectively.

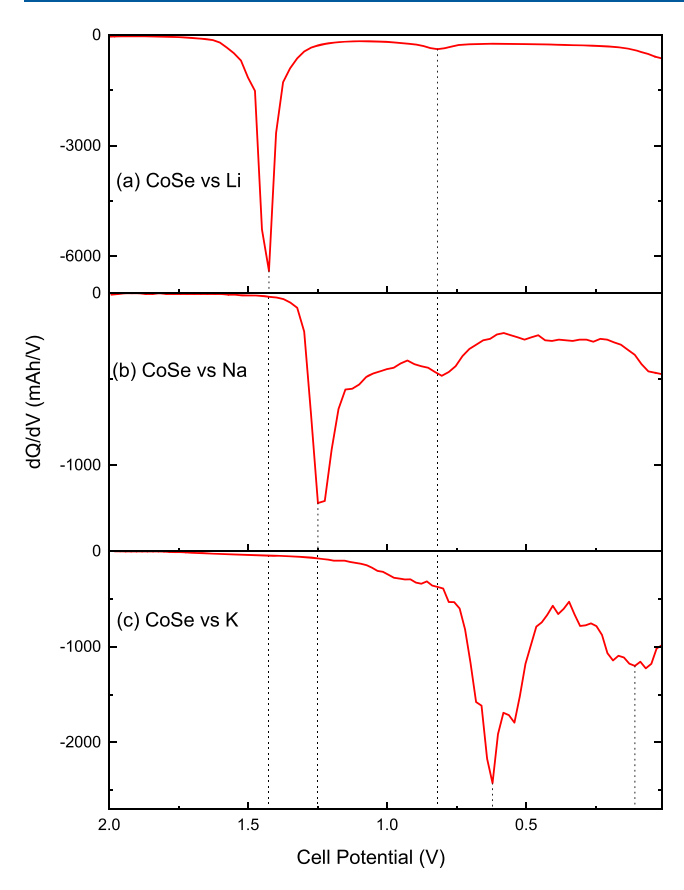


Figure 3. Differential capacity versus voltage plot for CoSe versus (a) Li, (b) Na, and (c) K half cells.

minimal capacity fade.<sup>2–4</sup> This discrepancy is likely attributable to the application of nanostructuring and/or narrow voltage windows in these studies.<sup>2–4</sup> It should be noted that crystalline electrodes were used in this work because the focus is on structural evolution, and increased crystallite size improves the

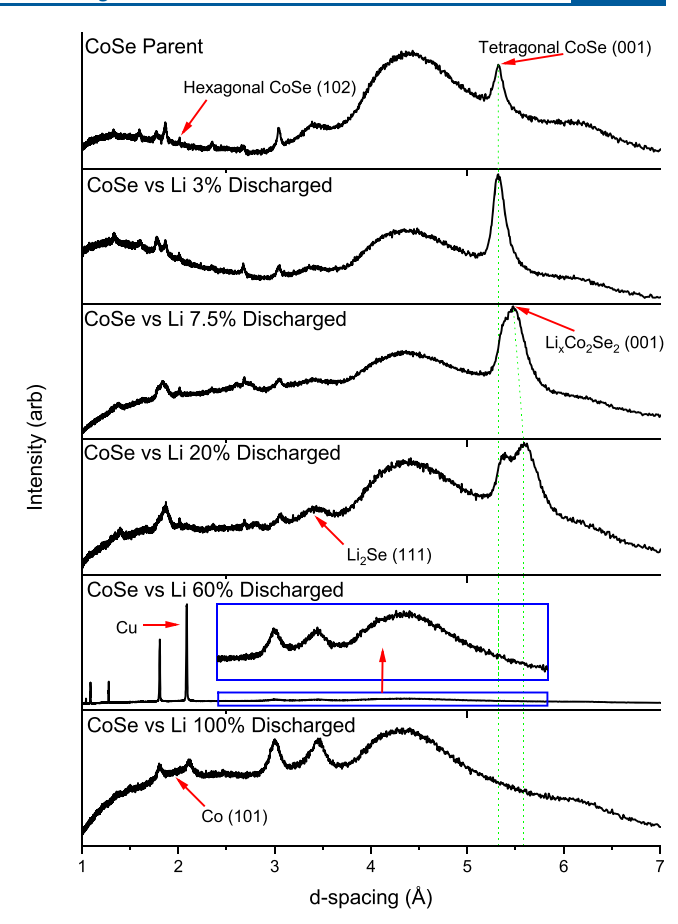


Figure 5. PXRD data from CoSe versus Li ex situ experiments, with key reflections indicated.

PXRD quality for structural analysis. The applicability of potential windows and/or nanosizing to CoSe is not investigated here but is suggested as a topic for future works.

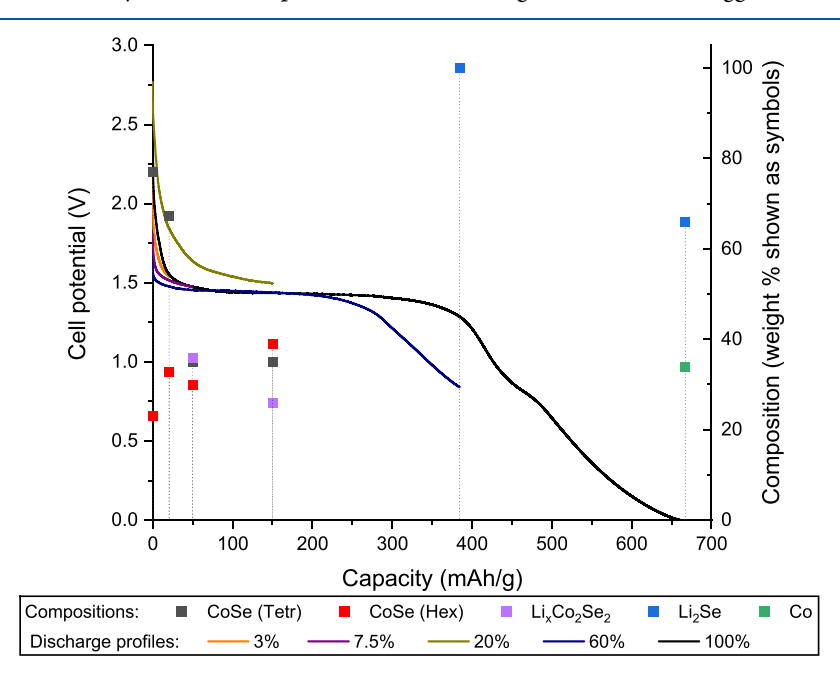
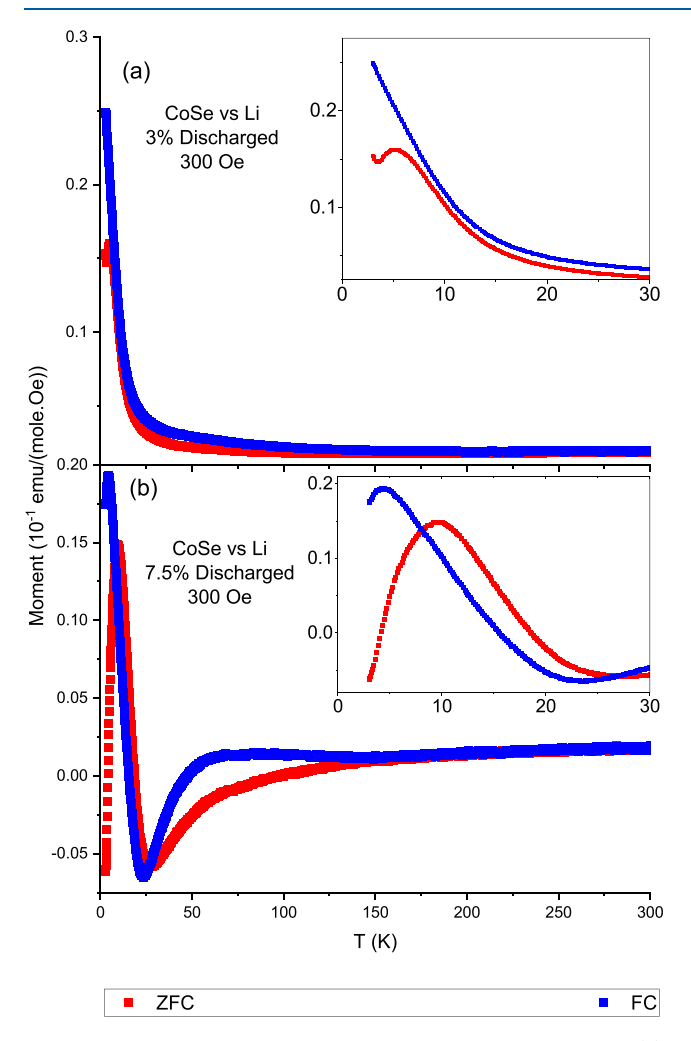


Figure 4. Discharge profiles (left axis) and weight percentages (right axis) for CoSe versus Li ex situ experiments. Uncertainties were calculated for the weight fractions; however, their magnitudes were smaller than the size of the datapoint markers.

Table 2. Lattice Parameters of Tetragonal CoSe and Selected Phases and Weighted Residuals from Rietveld Analyses of PXRD Data from CoSe versus Li Ex Situ Experiments

sample	CoSe a (Å)	CoSe c (Å)	$\text{Li}_{x}\text{Co}_{2}\text{Se}_{2}\ a\ (\text{Å})$	$\text{Li}_x\text{Co}_2\text{Se}_2$ $c$ (Å)	Li <sub>2</sub> Se a (Å)	Co <i>a</i> (Å)	Co c (Å)	wR
electrode	3.712(2)	5.330(3)						2.96%
3%	3.709(2)	5.337(2)						2.46%
7.5%	3.657(4)	5.373(4)	3.695(5)	5.509(4)				2.71%
20%	3.687(6)	5.383(8)	3.73(1)	5.605(9)				2.65%
60%					6.003(8)			6.59%
100%					6.014(4)	2.513(6)	4.08(1)	2.03%



**Figure 6.** Magnetic susceptibility of CoSe versus Li discharged to (a) 3% and (b) 7.5%, versus temperature, measured in an applied field of 300 Oe. Insets show magnified low temperature regions.

The operating voltage of the three systems fell principally within the 0–2 V range, suggesting a possible application as anode materials for alkali ion batteries. In order to briefly investigate the economic feasibility of this prospect, the performance and price of CoSe was compared to established anode materials for each category of battery. Compared to graphite, which is as an anode widely used in lithium-ion batteries, the hexagonal form of CoSe is 10 times more expensive. Regarding performance, 100th cycle discharge capacities of 250, 200, and 210 mAh/g have been reported for Li, Na, and K ion batteries, respectively, using graphite or expanded graphite. Regarding performancy using graphite or expanded graphite. These significantly exceeded the 50th cycle discharge capacities for CoSe reported in this work, which were 156, 13, and 15 mAh/g for Li, Na, and K half cells,

respectively. This comparison indicates that unmodified CoSe is not an economically viable replacement for incumbent alkaliion battery anode materials.

The discharge profiles for all systems exhibited a sharp initial drop in voltage, followed by a plateau region (in the case of K this exhibited a slight downward slope throughout), and finally a region of gradual voltage decrease. These features suggested the occurrence of three distinct reactions. The formulation of differential capacity–voltage plots in the range of 0-2 V (Figure 3) showed a sharp feature corresponding to the end of the plateau-like region for each system. Additionally, a second smaller feature was observed at  $\sim\!0.81$  V for Li and Na and at 0.11 V for K. Interestingly, the capacity at which the large sharp feature occurs is inversely correlated with ion size.

**CoSe versus Li Ex Situ Experiments.** Ex situ PXRD experiments were performed on CoSe versus Li half cells, which were discharged to the extents depicted in Figure 4. Rietveld analysis was performed with models using resultant PXRD data, and the calculated weight fractions of the phases present are also shown in Figure 4. A table with model parameters and detailed figures showing the Rietveld refinements for each sample are provided in the Supporting Information (Table S1 and Figures S3—S10, respectively). It should be noted that the PVDF and carbon black structural models were not included in refinements to avoid overparametizing the models.

The 3% sample (Figures S3 and S4) exhibited no new reflections compared to the parent; however, a very small shift in peak positions was observed, as shown in Figure 5. Rietveld refinement of the tetragonal CoSe structural model revealed no statistically significant change in the *a* lattice parameter, and a very slight increase in the *c* lattice parameter, as shown in Table 2. An angular-dependent variance in peak width was observed, so the microstrain parameter was refined, resulting in an improved fit. A correlation between microstrain and intercalation has been reported in the literature, <sup>26</sup> possibly suggesting the occurrence of insertion in this sample. A similar correlation was observed in this work, with microstrain observed for all CoSe versus Li samples, increasing in extent with the degree of discharge.

The 7.5% discharged sample (Figures S5 and S6) displayed the formation of a set of reflections slightly offset from those attributable to the parent at slightly higher *d*-spacings. These new reflections were consistent with the formation of a second, expanded phase of CoSe, likely Li<sub>x</sub>Co<sub>2</sub>Se<sub>2</sub>. The *c* lattice parameters of this new phase were significantly expanded compared to the parent while the *a* lattice parameter slightly shrank. It is unclear whether this phase separation is an intrinsic mechanism or related to the reaction front in the electrode. Further experiments with electrodes of varying thicknesses may resolve this, and such investigations are recommended for future works. Additionally, the original CoSe

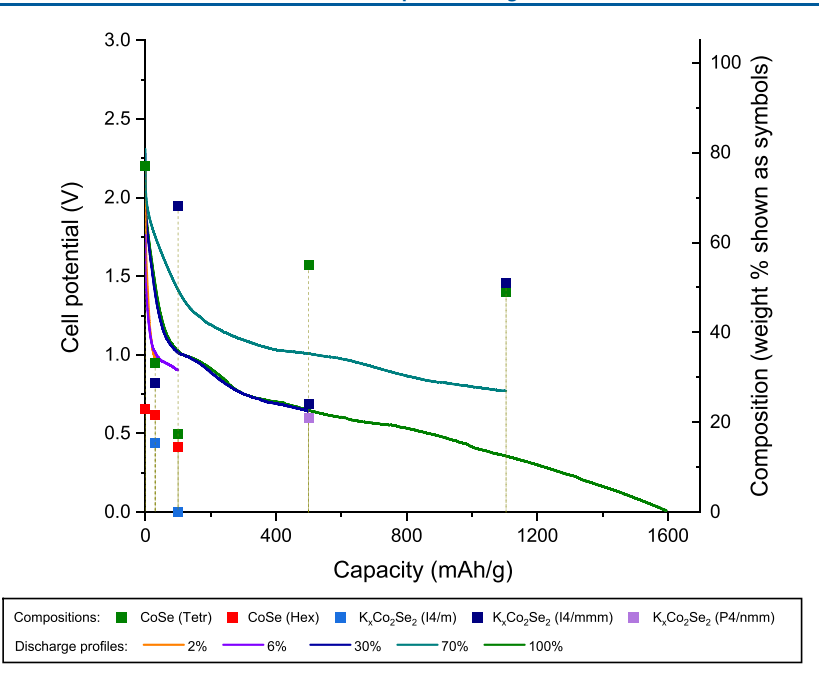
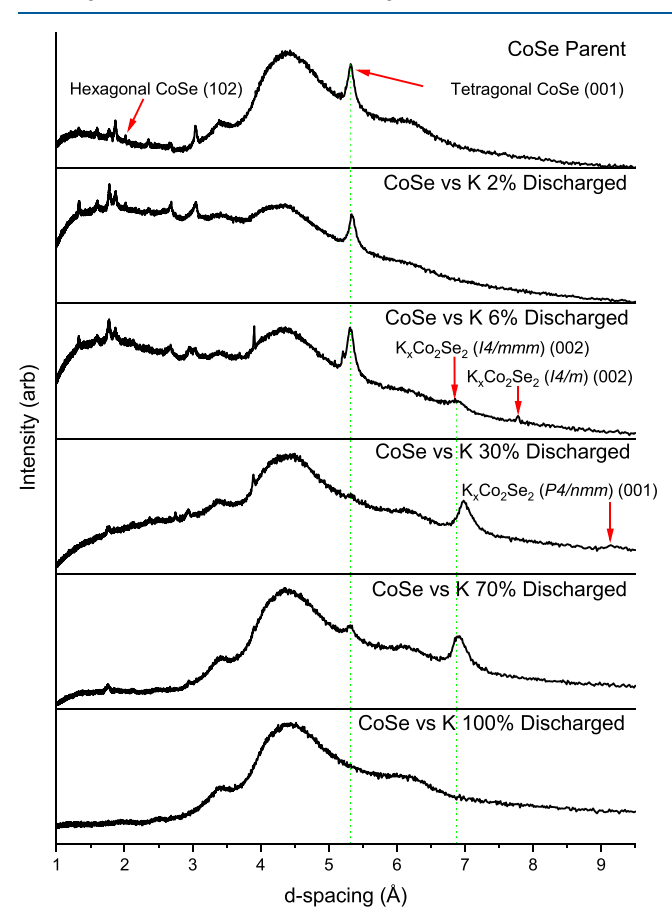


Figure 7. Discharge profiles (left axis) and weight percentages (right axis) for CoSe versus K ex situ experiments. Uncertainties were calculated for the weight fractions; however, their magnitudes were smaller than the size of the datapoint markers.



**Figure 8.** PXRD data from CoSe versus K ex situ experiments, with key reflections indicated.

phase at 7.5% discharge showed a slight expansion in the *c* lattice parameter and a contraction of the *a* lattice parameter relative to the 3% sample, suggesting that Li intercalation may have also occurred in this phase, albeit to a lower extent.

The 20% sample (Figures S7 and S8) showed no additional reflections compared to the 7.5% sample; however, both phases exhibited further expansion of the *c* lattice parameter. They also featured expansion of the *a* lattice parameter, which was consistent with continued intercalation of Li. Interestingly, it appears that the *c* lattice parameter consistently expanded with Li insertion, while the *a* lattice parameter contracted between 0 and 7.5% and then expanded from 7.5 to 20%. The trend exhibited by these results suggested that the initial region of the discharge profile corresponded to intercalation reactions:

$$x'Li^+ + x'e^- + 2CoSe \rightarrow Li_{x'}Co_2Se_2$$
 (3)

$$Li_{x'}Co_2Se_2 + xLi^+ + xe^- + 2CoSe$$

$$\rightarrow Li_{x'}Co_2Se_2 + Li_{x}Co_2Se_2, \text{ where } x > x'$$
(4)

It should be noted that the hexagonal CoSe phase (omitted from Table 2 for clarity but presented in Table S1) showed no statistically significant change in lattice parameters. The intensity and phase fraction (Figure 4) of the reflections attributable to this phase also appeared to remain relatively stable between 0 and 20% discharge. This trend, in conjunction with the decreased intensity and phase fraction of the tetragonal CoSe peaks and concomitant increase in the Li<sub>x</sub>Co<sub>2</sub>Se<sub>2</sub> phase fraction (see Figure 4), suggested that the majority of the intercalation occurred within the tetragonal CoSe phase. The endpoint of the initial downward sloped region in the discharge curves showed slight variation between samples, possibly due to loading or particle size differences. A value of 50 mAh/g was typical, corresponding to the intercalation of 0.26 Li atoms per functional unit. It should be noted that the 20% discharged sample exhibited an anomalous discharge profile, in which the initial sloped region persisted to a greater extent than in the other samples. The capacity of this sample corresponded to the insertion of 0.73 Li atoms per functional unit.

Table 3. Lattice Parameters of Tetragonal CoSe and Selected Phases and Weighted Residuals from Rietveld Analyses of PXRD Data from CoSe versus K Ex Situ Experiments

sample	CoSe a (Å)	CoSe c (Å)	$K_xCo_2Se_2$ (I4/mmm) $a$ (Å)	$K_x \text{Co}_2 \text{Se}_2$ (I4/mmm) $c$ (Å)	$K_x$ Co <sub>2</sub> Se <sub>2</sub> (I4/m) a (Å)	$K_x \text{Co}_2 \text{Se}_2$ (I4/m) c (Å)	$K_x \text{Co}_2 \text{Se}_2$ (P4/nmm) $a$ (Å)	$K_x \text{Co}_2 \text{Se}_2$ (P4/nmm) $c$ (Å)	wR
electrode	3.712(2)	5.330(3)							2.96%
2%	3.705	5.330	3.775	14.02	8.86	15.66			2.04%
6%	3.705(3)	5.330(2)	3.775(6)	14.02(3)	8.86(4)	15.66(2)			1.97%
30%	3.71(5)	5.3(1)	3.756(8)	14.09(1)			3.837(5)	9.24(2)	2.94%
70%	3.72(1)	5.33(4)	3.80(2)	13.9(1)					4.52%

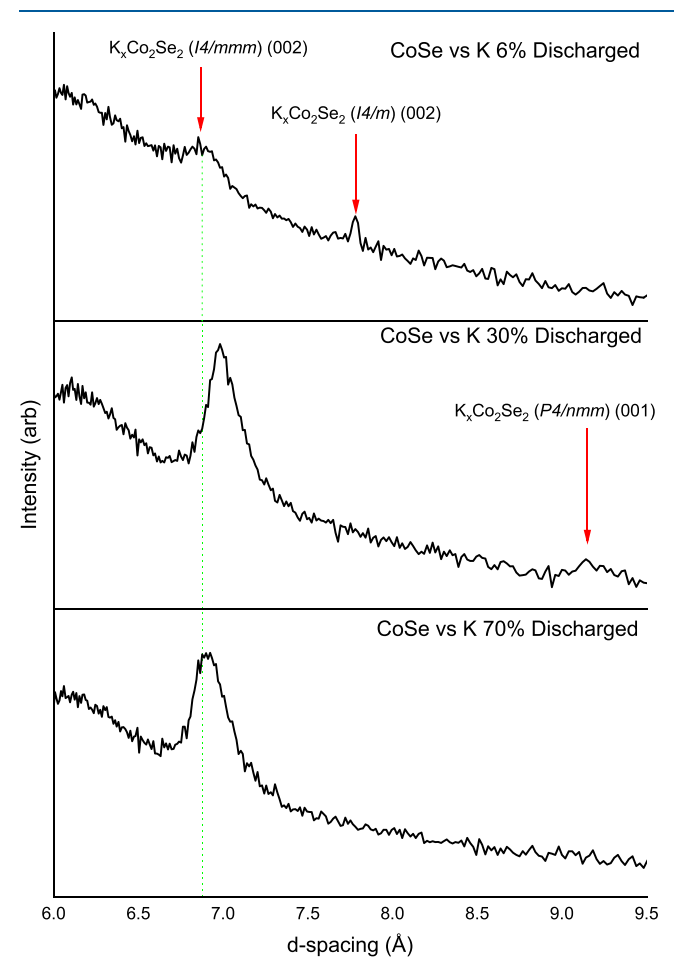


**Figure 9.** PXRD data from selected CoSe versus K ex situ experiments, zoomed to the region of interest, with key reflections indicated.

The reflections attributable to the original, lithiated, and hexagonal CoSe phases were not present in the 60% discharged sample (Figure S9). A new set of reflections were observed, which were found to be consistent with the formation of Li<sub>2</sub>Se with the space group  $Fm\bar{3}m$ . The 100% discharged sample (Figure S10) showed a similar set of reflections to those in the 60% sample and also a second set of reflections, which were found to be consistent with the presence of Co with space group  $P6_3/mmc$ . The Co reflections were broader than those attributable to Li<sub>2</sub>Se, suggesting this species was amorphous or nanosized. Taken together, these results are consistent with the occurrence of a conversion reaction:

$$\text{Li}_x \text{Co}_2 \text{Se}_2 / \text{Li}_{x'} \text{Co}_2 \text{Se}_2 + (4 - x/x') \text{Li}^+ + (4 - x/x') \text{e}^-$$
  
 $\rightarrow 2 \text{Li}_2 \text{Se} + 2 \text{Co}$  (5)

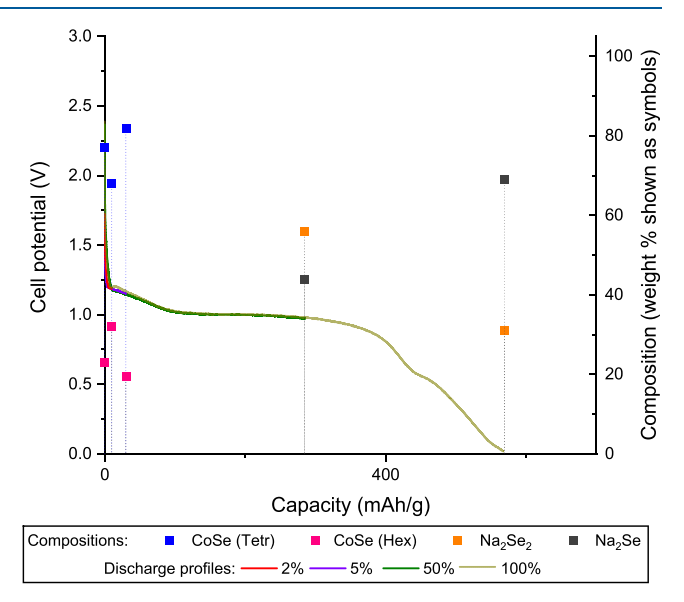


Figure 10. Discharge profiles (left axis) and weight percentages (right axis) for CoSe versus Na ex situ experiments. Uncertainties were calculated for the weight fractions; however, their magnitudes were smaller than the size of the datapoint markers.

This result is in agreement with previous studies on anti-PbO-type layered metal dichalogenides, which reported analogous conversion reactions.<sup>2–4,18</sup> The capacity of the second sloping region in the 100% discharge profile was approximately 350 mAh/g, which corresponds to a reaction consumption of 1.8 Li atoms. Consequently, these results suggest that the second downward sloped region corresponded to, or was dominated by, the conversion reaction.

It should be noted that the PXRD data collected from the 60% sample exhibited peaks attributable to the Cu current collector, as this sample could not be removed from the current collector. This inseparability was attributable to stronger adhesion, possibly due to a slight difference in loading. Consequently, the Cu structural model was refined during the Rietveld analysis, in addition to the Li<sub>2</sub>Se model. Specifically, the domain size, phase fraction, lattice parameters, and preferred orientation of this phase were refined. The lattice parameters exhibited only a very slight change from literature values, as expected. The resulting refinement exhibited close agreement with the observed data, as shown in Figure S9. The possibility that the Cu peaks obscured data from Li<sub>2</sub>Se or CoSe was also considered. However, comparison of the reflection positions from these phases indicated that they were not coincident with those of Cu.

Taken together, the results of these ex situ experiments suggest that the initial region and the pseudo-plateau/final region corresponded to intercalation and conversion reactions, respectively. The combined capacity of typical initial and final

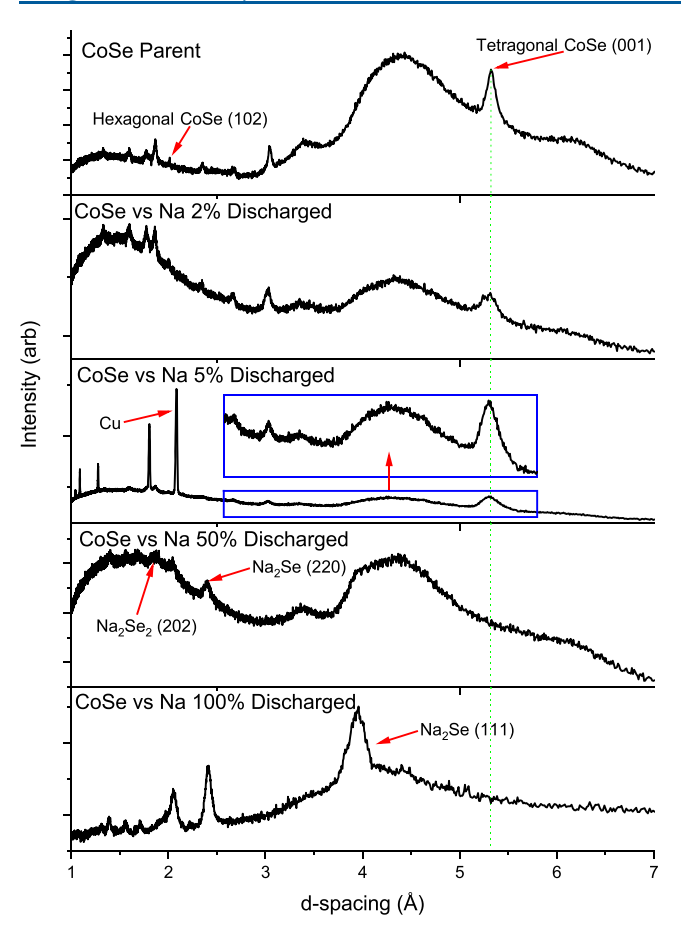
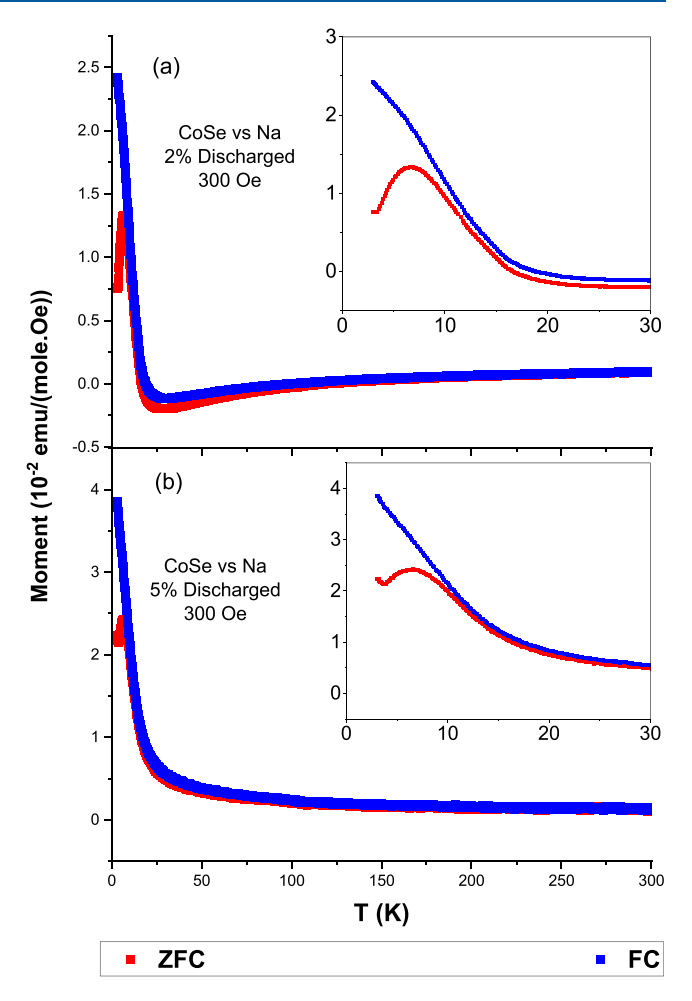


Figure 11. PXRD data from CoSe versus Na ex situ experiments, with key reflections indicated.

sloped regions or the initial and pseudo-plateau regions are both approximately 400 mAh/g, which is similar to the theoretical capacity of 389 mAh/h, based on the transfer of 2 Li ions. Besides SEI formation and other side reactions, a possible scenario could be that the increasing size of Co nanoparticles deposited at the end of the pseudo-plateau region followed their lithiation leading to  $\text{Li}_x\text{Co}$  alloys, e.g., via the surface and at the nanosized scale and therefore not detectable by PXRD.

The present work focused on the phase evolution associated with the first discharge process; however, a preliminary investigation into the evolution during subsequent cycles was performed. Specifically, ex situ PXRD was performed on a cell that had been cycled (discharged, then charged) five times with the XRD data collected at the fifth charged state. The capacity—voltage curves are presented in Figure S23 and Rietveld analysis in Figure S24. No peaks corresponding to CoSe were observed (as potentially anticipated at the charged



**Figure 12.** Magnetic susceptibility of CoSe versus Na discharged to (a) 2% and (b) 5%, versus temperature, which is measured in an applied field of 300 Oe. Insets show magnified regions near TC.

state) but two broad peaks consistent with  $\rm Li_2Se$  were observed, suggesting some degree of irreversibility of the conversion reaction.

The influence of Li intercalation on the magnetic properties of CoSe was investigated by performing magnetometry on the 3 and 7.5% discharged samples. The ZFC and FC profiles of the 3% sample, presented in Figure 6a, were similar to those previously reported for the parent material. Specifically, these were consistent with Pauli paramagnetism at high temperatures and ferromagnetism at low temperatures, with a Curie temperature of approximately 10 K. This suggested that the degree of Li intercalation present in the 3% sample induced minimal changes to the magnetic properties of CoSe.

The 7.5% sample, presented in Figure 6b, exhibited an unusual intercrossing of ZFC and FC profiles, at approximately

Table 4. Lattice Parameters of Tetragonal CoSe and Selected Phases and Weighted Residuals from Rietveld Analyses of PXRD Data from CoSe versus Na Ex Situ Experiments

sample	CoSe a (Å)	CoSe c (Å)	Na <sub>2</sub> Se a (Å)	Na <sub>2</sub> Se <sub>2</sub> a (Å)	$Na_2Se_2$ $c$ (Å)	wR
electrode	3.712(2)	5.330(3)				2.96%
2%	3.588(9)	5.31(1)				2.16%
5%	3.608(6)	5.251(7)				3.54%
50%			6.78(2)	4.74(7)	10.47(3)	2.29%
100%			6.809(4)	5.0(2)	11.15(1)	4.72%

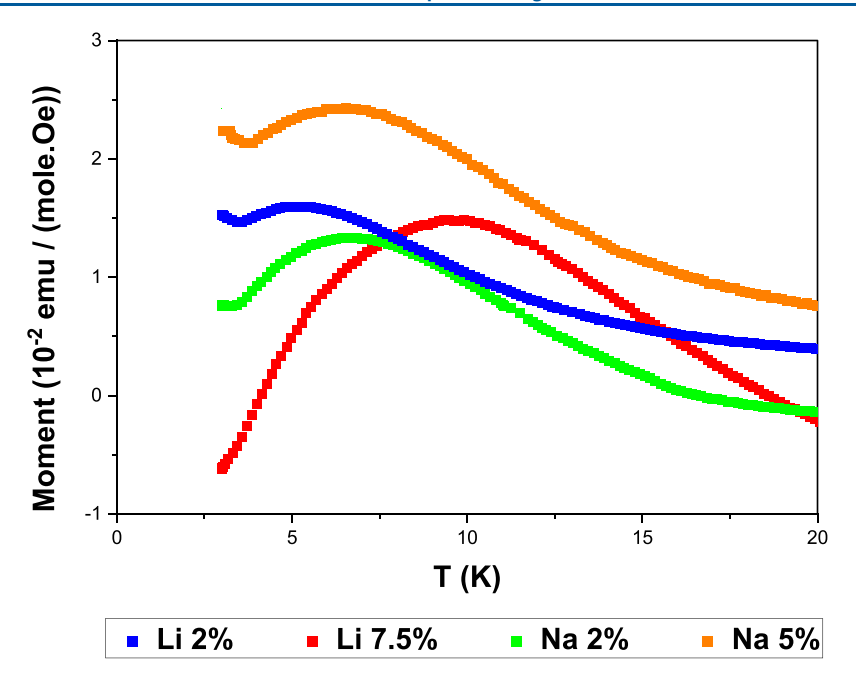


Figure 13. Overlaid ZFC curves of CoSe discharged to specified capacities against Li and Na.

10 K. Past research has attributed intercrossing of ZFC and FC profiles to the competition between ferromagnetic and antiferromagnetic phases. 27,28 Consequently, one possible explanation for this result is the formation of an antiferromagnetic Li<sub>x</sub>CoSe phase. However, a second possibility is the formation of a filamentary superconducting phase. Resistivity versus temperature experiments are required to resolve this, and such experiments are recommended for future works. It should be noted that due to the phase separation induced by electrochemical insertion (eq 4), the resultant data will require careful interpretation. Further experiments with techniques such as scanning electron microscopy or Raman spectroscopy may enable additional insights into the structural and morphological evolution. Such experiments are recommended for future works.

**CoSe versus K Ex Situ Experiments.** CoSe versus K ex situ PXRD experiments were performed at the depths of discharge shown in Figure 7, resulting in the XRD data shown in Figure 8. A table with model parameters and detailed Supporting Information (Table S2 and Figures S11–S16, respectively).

Tetragonal CoSe was present until approximately 70% discharge but showed essentially no significant change in lattice parameters, as shown in Table 3. The 2% (Figures S11 and S12) and 6% (Figures S13 and S14) discharged samples exhibited several additional peaks, which were found to be consistent with the formation of K<sub>r</sub>Co<sub>2</sub>Se<sub>2</sub> with the I4/mmm and the I4/m space groups. These two new phases corresponded to intercalation of K in the tetrahedral and octahedral void spaces. It should be noted that the additional reflections from the K<sub>r</sub>Co<sub>2</sub>Se<sub>2</sub> phases in the 2% sample were of low intensity; however, importing the K<sub>x</sub>Co<sub>2</sub>Se<sub>2</sub> structural models derived from the 6% sample resulted in a good statistical and visual fit. Furthermore, for the 2 and 6% cases, a graphite structural model was included to model carbon black. This is because the I4/m K<sub>x</sub>Co<sub>2</sub>Se<sub>2</sub> phase had a reflection marker that aligned with the intensity attributable to carbon black. For all other refinements in this work, carbon black was omitted in order to avoid over-parameterizing the model.

It should be noted that the PXRD data collected from the 6% sample contained peaks attributable to Cu. Consequently, the Cu structural model was refined during the Rietveld analysis, resulting in close agreement with the observed data, as shown in Figure S19. The Cu peak positions did not coincide with those of the CoSe or  $K_x$ CoSe phases, so this did not interfere with the refinement.

The 30% sample (Figure S15) exhibited the disappearance of the I4/m  $K_x$ Co<sub>2</sub>Se<sub>2</sub> and hexagonal CoSe reflections and the appearance of several additional reflections. The largest of these was observed at a d-spacing of 9.2 Å and was found to be consistent with the formation of a P4/nmm phase of  $K_x$ Co<sub>2</sub>Se<sub>2</sub>, which has two staggered K layers between the CoSe lamellae. The a and c lattice parameters of this new phase were 3.84 and 9.24 Å, respectively, which resembled those reported for the case of P4/nmm  $K_{0.51}$ Fe<sub>0.698</sub>Se, which were 3.89 and 9.19 Å respectively. The disappearance of the I4/m phase is consistent with the occurrence of a secondary intercalation reaction, in which a second layer of K ions intercalate within the Van der Waals gap, producing the P4/nmm phase, as per egs 6 and 7.

$$xK^{+} + xe^{-} + 2CoSe \rightarrow K_{x}Co_{2}Se_{2} (I4/m)$$
 (6)

$$x'K^{+} + x'e^{-} + K_{x}Co_{2}Se_{2}(I4/m)$$

$$\rightarrow K_{x+x'}Co_{2}Se_{2}(P4/nmm)$$
(7)

The disappearance of the reflections attributable to hexagonal CoSe is consistent with the reaction of this phase with K to form *I4/mmm* K<sub>x</sub>Co<sub>2</sub>Se<sub>2</sub>. It should be noted that hexagonal CoSe has been shown to react with K to produce *I4/mmm* K<sub>x</sub>Co<sub>2</sub>Se<sub>2</sub>—this reaction was the initial step in the synthesis of the tetragonal CoSe used in this work. Compared to the 6% sample, the *I4/mmm* K<sub>x</sub>Co<sub>2</sub>Se<sub>2</sub> phase showed very slight expansion and contraction of the *a* and c lattice parameters, respectively.

The evolution of the  $K_xCo_2Se_2$  phases is highlighted in Figure 9, in which a key region of the PXRD data for the 6, 30, and 70% samples is presented. The 70% discharged sample

(Figure S16) exhibited reflections attributable to tetragonal CoSe and I4/mmm K<sub>r</sub>Co<sub>2</sub>Se<sub>2</sub>; however, the P4/nmm reflections were not present. The disappearance of the P4/ nmm K<sub>x</sub>Co<sub>2</sub>Se<sub>2</sub> phase in the 70% sample is likely attributable to eq 8, with this phase undergoing conversion first due to its higher K content. This result was analyzed in conjunction with the 100% discharged sample, in which no reflections were present. As with the Li series, the K series showed an increase in the peak widths with discharge and an essentially amorphous or nanocrystalline sample at 100% discharge. This is likely attributable to granular fracturing due to volume changes brought on by phase evolution during discharge. The large discharge capacity of the K discharge cell suggests the occurrence of further reactions, in addition to phase separation and intercalation. Based on the results of the Li system, we speculate that an analogous conversion reaction with nanocrystalline products may have occurred, as shown in eq 8.

$$K_{x+x'}Co_2Se_2 + (4 - x - x')K^+ + (4 - x - x')e^-$$
  
 $\rightarrow 2K_2Se + 2Co$  (8)

**CoSe versus Na Ex Situ Experiments.** CoSe versus Na ex situ PXRD experiments were performed at the states shown in Figure 10. A table with model parameters and detailed figures showing the Rietveld refinements for each sample are provided in the Supporting Information (Table S3 and Figures S7—S22, respectively).

The 2% (Figures S17 and S18) and 5% (Figure S19) samples showed no additional reflections compared to the parent, as illustrated in Figure 11. In contrast to the Li and K systems, slight decreases in the a and c lattice parameters were observed, as presented in Table 4. This suggests that intercalation may have occurred, inducing contraction in the host lattice. Although this trend is unusual, we have observed a similar contraction in our previous work on the  $\mathrm{Bi}_2\mathrm{Te}_3$  versus Li and K systems. These results suggest that the initial downward sloping region of the discharge profile corresponds to the intercalation reaction shown in eq 9.

$$CoSe + Na^{+} + e^{-} \rightarrow Na_{x}CoSe$$
 (9)

In the 50% discharged sample (Figure S20), the parent reflections completely disappeared, and new reflections consistent with the formation of Na<sub>2</sub>Se<sub>2</sub> and Na<sub>2</sub>Se appeared. The 100% sample (Figure S21) showed the same set of reflections; however, an increase in the relative intensity of the Na<sub>2</sub>Se peaks was observed. This suggested the occurrence of the following reactions shown in eqs 10 and 11.

$$2\text{Na}_x\text{CoSe} + (2 - x)\text{Na}^+ + (2 - x)\text{e}^- \rightarrow \text{Na}_2\text{Se}_2 + 2\text{Co}$$
(10)

$$Na_2Se_2 + 2Na^+ + 2e^- \rightarrow 2Na_2Se$$
 (11)

Although eq 10 indicates the formation of Co, no reflections consistent with this species were observed. Consequently, we speculate that a nanosized or amorphous phase of this material was formed. The Na<sub>2</sub>Se<sub>2</sub> weight fraction decreased between the 50 and 100% discharged samples, as illustrated in Figure 10. This suggested that the reaction shown in eq 10 occurred initially, followed by that shown in eq 11.

In order to investigate the influence of Na intercalation on the magnetic properties of CoSe, magnetic measurements were performed on the 2 and 5% discharged samples. It should be noted that in contrast to the Li-inserted samples, the Nainserted samples did not exhibit the formation of multiple phases. The ZFC and FC profiles of the 2% discharged sample, presented in Figure 12a, exhibited a strong diamagnetic response, with a transition temperature of approximately 7.5 K. By contrast, the 5% discharged sample, presented in Figure 12b, exhibited a less pronounced diamagnetic response, with a similar transition temperature. One possible explanation for these results is that a superconducting Na<sub>x</sub>CoSe phase was formed in the 2% sample, and that the increased Na content in the 5% sample suppressed or eliminated this property. However, it is also possible that the diamagnetic response observed in the 2% discharged sample was due to the presence of a diamagnetic impurity. This uncertainty may be resolved by resistivity versus temperature measurements, and these are recommended for future works.

To summarize the trends observed in this work, both Na discharged samples and the 2% Li discharged sample exhibited similar, minor changes in their magnetic properties. However, the 7.5% Li discharged sample exhibited significantly modified magnetic properties. This is illustrated in Figure 13, in which the ZFC curves from each sample are overlaid. A more complete understanding of the effects of Na and Li intercalation on the magnetic properties may be achieved by discharging additional CoSe samples to different states. Consequently, such experiments are proposed for future works.

### CONCLUSIONS

The behavior of CoSe as an electrode material for alkali ion batteries was examined. High first discharge capacities of 957, 657, and 972 mAh/g were exhibited by the Li, Na, and K systems, respectively. However, cyclability was poor, with capacity fades of 52, 85, and 95% after the 10th cycle. Although the 50th cycle capacity of the Li system was the most favorable, at approximately 150 mAh/g, CoSe is more expensive than graphite by a factor of 10, likely rendering it uneconomical. The phase evolution of each system was investigated using ex situ PXRD in conjunction with the observed discharge profiles and capacities. For all systems, the reaction mechanism involved intercalation followed by conversion reactions. Interestingly, for the case of Na, the intercalation reaction was associated with a contraction in the stacking axis lattice parameter. Magnetometry was performed on the resultant Li<sub>x</sub>Co<sub>2</sub>Se<sub>2</sub> and Na<sub>x</sub>Co<sub>2</sub>Se<sub>2</sub> phases and indicated that intercalation modified the magnetic properties. Future works are proposed to further investigate the magnetic properties of these phases, specifically measurements of resistivity.

## ASSOCIATED CONTENT

## Supporting Information

The Supporting Information is available free of charge at https://pubs.acs.org/doi/10.1021/acs.inorgchem.1c00226.

Tables with comprehensive Rietveld refinement parameters and detailed figures of Rietveld analyses (PDF)

## AUTHOR INFORMATION

#### **Corresponding Author**

Neeraj Sharma – School of Chemistry, University of New South Wales, Sydney, NSW 2052, Australia;

Email: neeraj.sharma@unsw.edu.au

## **Authors**

Conrad H. R. Gillard – School of Chemistry, University of New South Wales, Sydney, NSW 2052, Australia

Xiuquan Zhou — Department of Chemistry and Biochemistry, University of Maryland, College Park, Maryland 20742, United States; orcid.org/0000-0002-1361-3880

Maxim Avdeev — Australian Nuclear Science and Technology Organisation, Kirrawee DC, NSW 2232, Australia; School of Chemistry, The University of Sydney, Sydney, NSW 2006, Australia; ◎ orcid.org/0000-0003-2366-5809

Efrain E. Rodriguez – Department of Chemistry and Biochemistry, University of Maryland, College Park, Maryland 20742, United States; orcid.org/0000-0001-6044-1543

Complete contact information is available at: https://pubs.acs.org/10.1021/acs.inorgchem.1c00226

### Notes

The authors declare no competing financial interest. C.G. was supported by an Australian Government Research Training Program (RTP) Scholarship. C.G. would also like to thank AINSE Limited for providing financial assistance (award, PGRA). This work was financially supported by the Australian Research Council Discovery programs (DP200100959 and FT200100707). Research at the University of Maryland was supported by the NSF Career DMR-1455118.

## REFERENCES

- (1) Zhou, X.; Wilfong, B.; Vivanco, H.; Paglione, J.; Brown, C. M.; Rodriguez, E. E. Metastable layered cobalt chalcogenides from topochemical deintercalation. *J. Am. Chem. Soc.* **2016**, *138*, 16432–16442.
- (2) Zhong, D.; Chen, J.; Zhang, J.; Luo, Y.; Li, Z.; Cheng, L.; Chen, Y.; Wang, G.; Wang, R. The yolk-shell FeSe@C nanobox with novel synthesis and its high performance for the anode of lithium-ion batteries. *Materials Research Express* **2019**, *6*, No. 085058.
- (3) Xing, C.; Zhang, D.; Cao, K.; Zhao, S.; Wang, X.; Qin, H.; Liu, J.; Jiang, Y.; Meng, L. In situ growth of FeS microsheet networks with enhanced electrochemical performance for lithium-ion batteries. *J. Mater. Chem. A* **2015**, *3*, 8742–8749.
- (4) Wei, D.; Liang, J.; Zhu, Y.; Hu, L.; Zhang, K.; Zhang, J.; Yuan, Z.; Qian, Y. Layer structured  $\alpha$ -FeSe: A potential anode material for lithium storage. *Electrochem. Commun.* **2014**, 38, 124–127.
- (5) Abe, H.; Noji, T.; Kato, M.; Koike, Y. Electrochemical Lintercalation into the Fe-based superconductor FeSe<sub>1-x</sub>Tex. *Phys. C* **2010**, 470, S487–S488.
- (6) Chen, D.; Wang, X.; Chen, J.; Ren, Z.; Xue, M.; Chen, G. Rewriting the Superconductivity in Iron-Based Superconductors by Lithium-Ion Insertion and Extraction. *Adv. Mater.* **2015**, 27, 4224–4228.
- (7) Kajita, T.; Kawamata, T.; Noji, T.; Hatakeda, T.; Kato, M.; Koike, Y.; Itoh, T. Electrochemical Na-intercalation-induced high-temperature superconductivity in FeSe. *Phys. C* **2015**, *519*, 104–107.
- (8) Burrard-Lucas, M.; Free, D. G.; Sedlmaier, S. J.; Wright, J. D.; Cassidy, S. J.; Hara, Y.; Corkett, A. J.; Lancaster, T.; Baker, P. J.; Blundell, S. J.; Clarke, S. J. Enhancement of the superconducting transition temperature of FeSe by intercalation of a molecular spacer layer. *Nat. Mater.* **2013**, *12*, 15–19.
- (9) Ying, T. P.; Chen, X. L.; Wang, G.; Jin, S. F.; Zhou, T. T.; Lai, X. F.; Zhang, H.; Wang, W. Y. Observation of superconductivity at 30 $\sim$  46 K in  $A_x$ Fe<sub>2</sub>Se<sub>2</sub> (A= Li, Na, Ba, Sr, Ca, Yb and Eu). *Sci. Rep.* **2012**, 2, 1–7.
- (10) Hatakeda, T.; Noji, T.; Kawamata, T.; Kato, M.; Koike, Y. New Li-Ethylenediamine-Intercalated Superconductor  $\text{Li}_x(C_2H_8N_2)$ -yFe<sub>2-x</sub>Se<sub>2</sub> with  $\text{T}_c=45$  K. J. Phys. Soc. Jpn. **2013**, 82, 123705.

- (11) Hosono, S.; Noji, T.; Hatakeda, T.; Kawamata, T.; Kato, M.; Koike, Y. New Intercalation Superconductor  $\text{Li}_x(C_6\text{H}_{16}\text{N}_2)_y\text{Fe}_{2-z}\text{Se}_2$  with a Very Large Interlayer-Spacing and  $\text{T}_c$ = 38 K. J. Phys. Soc. Jpn. **2014**, 83, 113704.
- (12) Hatakeda, T.; Noji, T.; Sato, K.; Kawamata, T.; Kato, M.; Koike, Y. New Alkali-Metal-and 2-Phenethylamine-Intercalated Superconductors  $A_x(C_8H_{11}N)_yFe_{1-2}Se$  (A= Li, Na) with the Largest Interlayer Spacings and  $T_c \sim 40$  K. J. Phys. Soc. Jpn. **2016**, 85, 103702.
- (13) Wilfong, B.; Zhou, X.; Vivanco, H.; Campbell, D. J.; Wang, K.; Graf, D.; Paglione, J.; Rodriguez, E. Frustrated magnetism in tetragonal CoSe, analogue to superconducting FeSe. *arXiv* **2017**, DOI: 10.1103/PhysRevB.97.104408.
- (14) Alekseeva, Å. M.; Drozhzhin, O. A.; Dosaev, K. A.; Antipov, E. V.; Zakharov, K. V.; Volkova, O. S.; Chareev, D. A.; Vasiliev, A. N.; Koz, C.; Schwarz, U.; Rosner, H.; Grin, Y. New superconductor  $\text{Li}_x\text{Fe}_{1+\delta}\text{Se}$  ( $x \le 0.07$ , T c up to 44 K) by an electrochemical route. *Sci. Rep.* **2016**, *6*, 25624.
- (15) Lu, X. F.; Wang, N. Z.; Zhang, G. H.; Luo, X. G.; Ma, Z. M.; Lei, B.; Huang, F. Q.; Chen, X. H. Superconductivity in LiFeO<sub>2</sub>Fe<sub>2</sub>Se<sub>2</sub> with anti-PbO-type spacer layers. *Phys. Rev. B* **2014**, 89, No. 020507.
- (16) Lai, X.; Zhang, H.; Wang, Y.; Wang, X.; Zhang, X.; Lin, J.; Huang, F. Observation of superconductivity in tetragonal FeS. *J. Am. Chem. Soc.* **2015**, *137*, 10148–10151.
- (17) Zhou, X.; Eckberg, C.; Wilfong, B.; Liou, S.-C.; Vivanco, H. K.; Paglione, J.; Rodriguez, E. E. Superconductivity and magnetism in iron sulfides intercalated by metal hydroxides. *Chem. Sci.* **2017**, *8*, 3781–3788.
- (18) Chen, G.-Y.; Sun, Q.; Yue, J.-L.; Shadike, Z.; Yang, Y.; Ding, F.; Sang, L.; Fu, Z.-W. Conversion and displacement reaction types of transition metal compounds for sodium ion battery. *J. Power Sources* **2015**, 284, 115–121.
- (19) Goodenough, J. B.; Park, K.-S. The Li-ion rechargeable battery: a perspective. J. Am. Chem. Soc. 2013, 135, 1167–1176.
- (20) Toby, B. H.; Von Dreele, R. B. GSAS-II: the genesis of a modern open-source all purpose crystallography software package. *J. Appl. Crystallogr.* **2013**, *46*, 544–549.
- (21) Aesar, A. 40224 Cobalt(II) selenide, 99+% (metals basis). https://www.alfa.com/en/catalog/040224/ (14 May),
- (22) Sigma-Aldrich Bismuth(III) telluride https://www.sigmaaldrich.com/catalog/product/aldrich/733482?lang=en&region=AU&cm\_sp=Insite-\_-caContent\_prodMerch\_cooccuranceModel-\_prodMerch10-1 (19 April),
- (23) Wen, Y.; He, K.; Zhu, Y.; Han, F.; Xu, Y.; Matsuda, I.; Ishii, Y.; Cumings, J.; Wang, C. Expanded graphite as superior anode for sodium-ion batteries. *Nature Commun.* **2014**, *5*, 1–10.
- (24) Fan, L.; Ma, R.; Zhang, Q.; Jia, X.; Lu, B. Graphite Anode for a Potassium-Ion Battery with Unprecedented Performance. *Angew. Chem., Int. Ed.* **2019**, *58*, 10500–10505.
- (25) Wu, Y.-P.; Rahm, E.; Holze, R. Carbon anode materials for lithium ion batteries. *J. Power Sources* **2003**, *114*, 228–236.
- (26) Fell, C. R.; Qian, D.; Carroll, K. J.; Chi, M.; Jones, J. L.; Meng, Y. S. Correlation between oxygen vacancy, microstrain, and cation distribution in lithium-excess layered oxides during the first electrochemical cycle. *Chem. Mater.* **2013**, *25*, 1621–1629.
- (27) Wang, H. O.; Zhao, P.; Sun, J. J.; Tan, W. S.; Su, K. P.; Huang, S.; Huo, D. X. Investigation of magnetic response of charge ordering in half-doped La<sub>0.5</sub>Ca<sub>0.5</sub>MnO<sub>3</sub> manganite. *J. Mater. Sci.* **2018**, 29, 13176–13179.
- (28) Wang, H.; Yang, W.; Su, K.; Huo, D.; Tan, W. Exchange-bias field induced by surface inhomogeneities in ferromagnetic/charge-ordered bilayer structure. *J. Alloys Compd.* **2015**, *648*, 966–970.
- (29) Shoemaker, D. P.; Chung, D. Y.; Claus, H.; Francisco, M. C.; Avci, S.; Llobet, A.; Kanatzidis, M. G. Phase relations in  $K_xFe_{2-y}Se_2$  and the structure of superconducting  $K_xFe_2Se_2$  via high-resolution synchrotron diffraction. *Phys. Rev. B* **2012**, *86*, 184511.
- (30) Gillard, C. H. R.; Jana, P. P.; Rawal, A.; Sharma, N. Electrochemical phase evolution of tetradymite-type Bi<sub>2</sub>Te<sub>3</sub> in lithium, sodium and potassium ion half cells. *J. Alloys Compd.* **2020**, 155621.